ACS OMEGA

Open Access

http://pubs.acs.org/journal/acsodf

Article

Unraveling Dimensional Tuning: From 2D to 3D in Covalent Organic Frameworks for Enhanced 2e⁻ Oxygen Reduction Reaction

Subhajit Bhunia, Linguo Lu,[▽] Suzatra Chatterjee,[▽] Mounesha Garaga, Alvaro Mayoral, Ashley R. Head, Steven G. Greenbaum, Zhongfang Chen, Xiaowei Wu, and Carlos R. Cabrera*

Cite This: *ACS Omega* 2025, 10, 18829−18839

Read Online

ACCESS | Metrics & More | Article Recommendations | Supporting Information

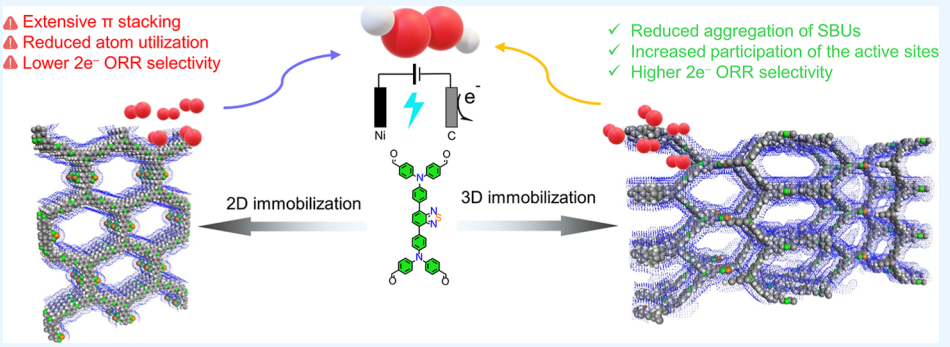

ABSTRACT: Covalent organic frameworks (COFs) with a two-dimensional (2D) topology have recently emerged as promising catalyst systems for the electrosynthesis of hydrogen peroxide (H_2O_2) from oxygen (O_2). However, designing 2D catalysts to achieve higher H_2O_2 selectivity presents a significant challenge because of the extensive layer stacking and the aggregated active sites located in the basal planes. It results in lower atom utilization, which requires attention. In this study, we present two functionally similar COFs: one with a 2D rhombus topology (2D@BT_TPA-COF) and another with a three-dimensional (3D) noninterpenetrated *pts* topology (3D@BT_TPA-COF). Both COFs were utilized for the 2e⁻ oxygen reduction reaction (2e⁻ ORR). Tunning the dimensionality from 2D to 3D resulted in an increase in H_2O_2 selectivity from approximately ∼56% to approximately ∼96% (at 0.4 V) and a rise in the turnover frequency (TOF) from 0.05 to 0.08 s^{-1} at 0.3 V. Nonaggregated active site distribution over 3D topology, featuring higher active site exposure, provides better access to the O_2/electrolyte and facilitates electron transfer leading to higher 2e⁻ ORR activity and selectivity compared to the 2D counterpart.

INTRODUCTION

Covalent organic frameworks (COFs) stand out as highly stable candidates in reticular chemistry, owing to their robust covalent bond-based connectivity.[1−6] Through a strategic selection of size, shape, and synthetic building units (SBUs), COFs exhibit a diverse range of topo structures, including both two-dimensional and three-dimensional configurations, offering a plethora of functionalities.[7−10] These structures find wide applications in various fields such as gas uptake,[11−14] catalysis,[15−21] energy storage[22−24] and conversion,[25,26] and chemo-sensing.[27] In recent trends, COFs have emerged as promising electrocatalysts for a range of electrochemical conversions, including the oxygen evolution reaction (OER),[28−30] oxygen reduction reaction (ORR),[31−33] carbon dioxide reduction reaction (CO_2RR),[34,35] nitrogen reduction reaction (NRR)[36] among others. The electrosynthesis of H_2O_2 through the selective 2e⁻ ORR is particularly interesting.

The electrochemical production of H_2O_2 offers an environmentally friendly approach with reduced production costs and waste generation, alongside easy separation processes compared to conventional methods such as the anthraquinone process. However, developing efficient electrocatalysts for H_2O_2 production poses challenges, primarily due to the competitive four-electron (4e⁻) ORR, which limits peroxide selectivity.[37] While noble metal-based alloys (Au−Pt, Ag−Hg, Pt−Hg, etc.)[38] have demonstrated high efficiency in H_2O_2 electrosynthesis, their cost, scarcity, and long-term corrosion drawbacks hinder widespread industrial adoption. To address these challenges, a metal-site isolation strategy has been proposed to enhance peroxide production with minimal metal usage.[39] Various metal-free catalyst systems have been synthesized using techniques such as surface oxidation, heteroatom doping, and defect introduction to achieve higher

Received: January 21, 2025
Revised: March 12, 2025
Accepted: April 10, 2025
Published: April 28, 2025

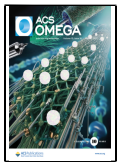

efficiency and selectivity.[40,41] However, these methods often lack designability, suffer from uncontrolled heteroatom installation, and exhibit lower atom utilizations. In this context, COFs offer a unique advantage with their precise designability via covalent bonds, enabling the accurate control of the edge-to-bulk heteroatom ratio by incorporating heterocyclic building units. Their higher crystallinity, interconnected porous structures, and chemical robustness make them ideal for establishing a three-phase interface (solid−liquid−gas) near the electrode area. While two-dimensional COFs are commonly reported as excellent electrocatalysts due to their facile charge/carrier transport compared to three-dimensional COFs, van der Waals (VdW) stacking hinders the exposure of base-plane-hosted atoms present in the 2D COF backbone. Recent studies by Hu et al. have shown that the edge atom-rich one-dimensional (1D) COFs exhibit better $2e^-$ ORR performance than extended 2D COFs.[42] In current trends, the synthesis of 3D COFs with various topologies has gained a broad scientific interest in the scientific community.[43] Employing 3D topology COFs has shown promise in overcoming limited atom utilization challenges, as reported by Jiang and colleagues in CO_2RR studies.[44] Herein, we demonstrate how the dimensionality of the COFs can influence their electrocatalytic activity. Specifically, we synthesized two chemically similar COFs (3D@BT_TPA-COF and 2D@BT_TPA-COF), featuring 3D periodic and 2D periodic topology, respectively. Both COFs were employed for $2e^-$ ORR electrocatalysis, revealing that the reticular modulation from 2D to 3D noninterpenetrated structures led to improved activity and selectivity for electrochemical H_2O_2 production. The noninterpenetrated 3D lattice provided higher exposure of active sites to electrolytes, provided a broader diffusion path for O_2 gas molecules, and resulted in higher peroxide production efficiency with improved selectivity.

MATERIALS AND METHODS

Synthesis of 3D@BT_TPA-COF. An 1,2 dichlorobenzene (*o*-DCB)/*n*-butanol (4/1 by vol.; 0.5 mL) mixture of BT_TPA (0.025 mmol, 18.2 mg), TAPM (0.025 mmol, 9.5 mg), $Sc(OTf)_3$ (∼0.5 mg, 0.04 equiv) in a glass ampule (2 mL) was degassed by three freeze−pump−thaw cycles. After that, the ampule was sealed off and heated to 100 °C for 5 days. Then the oven was cooled to room temperature at a constant cooling rate of 0.1 °C. The precipitates were collected by centrifugation and then washed with methanol and acetone (3 × 100 mL) until the colorless eluent was obtained. Then, the wet powder was transferred to the Soxhlet chamber for an extensive wash with methanol and THF for 2 days.

Synthesis of 2D@BT_TPA-COF. An *o*-DCB/Ethanol/AcOH (8 M) (4/1/1 by vol; 0.6 mL) mixture of BT_TPA (0.025 mmol, 18.2 mg) and PDA (0.025 mmol, 5.2 mg) in a glass ampule (2 mL) was degassed by three freeze−pump−thaw cycles. After that, the ampule was sealed off and heated to 95 °C for 4 days. Then the oven was cooled to room temperature and kept for 1 day. The precipitates were collected by centrifugation and then washed with methanol, THF, and acetone (3 × 100 mL) until the colorless eluent was obtained. Then, the wet powder was transferred to the Soxhlet chamber for an extensive wash with THF for 6 h. The sample was activated using hexane.

Material Characterization. Electron microscopy analyses were carried out in an FEI XFEG Titan operated at 300 kV. The column was equipped with a CEOS spherical aberration corrector for the electron probe, which was aligned before the experiments using a gold standard sample. The microscope was also fitted with an Oxford EDS detector and a Gatan Tridiem Energy Filter (GIF) for chemical analysis. The samples were prepared by dispersing the fine powders in absolute ethanol, and a few drops of the suspension were placed onto lacey carbon copper microgrids. Fourier transform infrared (FTIR) spectra were recorded on Spectrum One in the spectral range of 500−4000 cm^{-1} using the KBr disk method. The Brunauer−Emmett−Teller (BET) specific surface areas were calculated from the N_2 adsorption/desorption isotherm at 77 K (Autosorb-IQ-MP, USA) and the pore size distributions were calculated from density functional theory. Before analysis, the sample was degassed at 120 °C for 6 h. Solid-state ^{13}C cross-polarization magic angle spinning NMR (CP/MAS NMR) spectra were recorded at 400 MHz with an Advance III Bruker Corporation instrument. The XPS data were collected on a lab-based ambient pressure X-ray photoelectron spectrometer at the Center for Functional Nanomaterials at Brookhaven National Laboratory, Upton, NY. The instrument uses monochromated, focused Al K-alpha photons (1486.7 eV) and has a PHIOBOS 150 NAP hemispherical analyzer and 2D-delay line detector.[45] The spectra were collected under the pressure of argon gas to minimize the charging effects of the insulating samples. Binding energies were corrected for adventitious carbon (285.0 eV). The Powder X-ray diffraction (PXRD) data were collected on a PANalytical B.V. Empyrean powder diffractometer using a Cu Kα source (λ = 1.5418 Å) over the range 2θ = 2.0−40.0° with a step size of 0.02° and 2 s per step.

Electrochemical Measurements. The electrochemical oxygen reduction reaction (ORR) experiment of the COF catalysts (3D@BT_TPA-COF and 2D@BT_TPA-COF) was performed using a standard three-electrode system using a CHI 760E electrochemical workstation (CH Instruments, USA). Graphite rod was used as the counter electrode (CE) and the Ag/AgCl electrode (3 M KCl solution) was used as the reference electrode (RE). Catalyst was cast on a rotating ring disk electrode (RRDE, PINE Research Instrumentation, USA). All the potentials (V) were calibrated and converted to the reversible hydrogen electrode (RHE) using E (vs RHE) = E (vs Ag/AgCl) + 0.196 V + 0.059 × pH-iR. Before each measurement, the cleanness of the blank GC was first checked by scanning the CV at a scan rate of 50 mV s^{-1}. The current should only exhibit the shape of capacitance with a current density less than an order of magnitude below 10^{-7} A. Before casting the catalyst, the RRDE electrode was carefully polished with the alumina slurry (1 and 0.3 μm, respectively) and washed with water and ethanol. The ink was prepared as follows. At first, COFs (2 mg) were dispersed into the mixture of 980 μL of ethanol and 20 μL of Nafion solution (5 wt %) and sonicated for at least 45 min; 10 μL of the homogeneous ink was pipetted onto the RRDE electrode and dried at room temperature to generate a catalyst loading of ∼0.1 mg cm^{-2}. The electrolytic cell was filled with 0.1 M potassium hydroxide (KOH) electrolyte, presaturated with oxygen (O_2) by constant purging for at least half an hour. First, several circles of CVs (50 mV/s) were recorded until the curve was stable to get rid of the possible contaminant on the surface. The Pt ring was electrochemically cleaned from 0.6 to 0 V for 50 cycles at a scan rate of 300 mV s^{-1}. All of the electrochemical measurements were performed in an O_2-presaturated 0.1 M KOH solution. To detect the produced H_2O_2, a fixed potential

https://doi.org/10.1021/acsomega.5c00568
ACS Omega 2025, 10, 18829−18839

of 1.2 V vs RHE was set to the Pt ring electrode during the linear sweep voltammetry (LSV). LSV curves were collected at a scan rate of 10 mV s^{-1}.

The H_2O_2 selectivity and electron transfer number were calculated from the disk current and ring current results based on the following equations.

$$H_2O_2(\%) = 200 \times \frac{i_{ring}/N}{|i_{disk}| + i_{ring}/N} \quad (1)$$

$$n = 4 \times \frac{|i_{disk}|}{|i_{disk}| + i_{ring}/N} \quad (2)$$

where i_{disk} and i_{ring} are the disk and ring current, respectively, and N is the collection efficiency. Tafel slopes were calculated based on the Tafel equation

$$\eta = b\log(j/j_0) \quad (3)$$

where η is the overpotential, b is the Tafel slope, j is the current density, j_0 is the exchange current density. Electrochemical impedance spectroscopy (EIS) analysis was performed at open circuit potential (OCP) vs RHE with an oscillation amplitude of 5.0 mV and a frequency range from 0.1 to 10^6 Hz.

The diffusion of hydroxide ion (D_{OH^-}) was calculated by the following equation[46]

$$D_{OH^-} = \frac{R^2T^2}{2A^2n^4F^4C^2\sigma^2} \quad (4)$$

where R = gas constant (8.314 J K^{-1} mol^{-1}), T is the room temperature (298 K), A is the geometrical surface area of the GC electrode (0.196 cm^2), n is the number of electrons, F is the Faraday constant (96,485C mol^{-1}), and C is the concentration of OH^- (0.1 M). According to $Z' = R_s + R_{ct} + \sigma\omega^{-1/2}$ where ω is the angular frequency. σ can be determined from the slope of Z' vs $\omega^{-1/2}$ plot.

H-Cell Setup. Bulk electrosynthesis of H_2O_2 in 0.1 M KOH was carried out in a customized H-Cell electrolyzer with Toray carbon paper (1.5 × 1.5 cm^2) as the working electrode, Nickel foam as the counter electrode, and Ag/AgCl (saturated KCl) as the reference electrode. The LSV polarization curve of the samples was recorded at the scan rate of 50 mV s^{-1} in O_2-saturated electrolytes in the H-cell system. The anode and cathode chambers were separated by a Fumasep FAA-3-PK-130 anion exchange membrane (Fuel Cell Store). Typically, 100 μL of the catalyst ink was drop-cast on the surface (the loading density ~0.1 mg cm^{-2}). After electrocatalysis, $MgSO_4$ was added to the electrolyte to suppress decomposition.

The amount of H_2O_2 was quantitatively estimated by a colorimetric titration method

$$2Ce^{4+}(\text{Yellow}) + H_2O_2 \rightarrow 2Ce^{3+}(\text{Colorless}) + 2H^+ + O_2\uparrow \quad (5)$$

Before the ORR electrolysis started, The H_2O_2 concentration-absorbance (λ_{max} = 316 nm) curve was plotted by linear fitting of the absorbance values at wavelength length of 316 nm for various known concentrations of Ce^{4+} (up to 0.5 mM). Then, the appropriate amount of the electrolyte from the working electrode compartment was added to 4 mL of 0.5 mM Ce^{4+} stock solution and the absorbance at 316 nm was measured after standing for 2 h to determine the Ce^{4+} concentration. Based on the linear relationship between the absorbance (316 nm) and Ce^{4+} concentration, the molar amounts of consumed Ce^{4+} after the reaction could be calculated. The amounts of H_2O_2 produced can be estimated as half of the molar amounts of Ce^{4+} consumed. The Faradaic efficiency (FE) for H_2O_2 generation in the H-cell was calculated as follows

$$FE(\%) = 2 \times \frac{CVF}{Q} \quad (6)$$

where F is the Faraday constant (96,485C mol^{-1}), C is the concentration of H_2O_2, V is the volume of electrolyte, and Q is the total charge during the ORR.

The Mott−Schottky plot was recorded within the potential range of −0.4−+1.2 V vs RHE at the AC frequency range between 1000 and 2000 Hz and an amplitude of 5 mV in Ar-saturated 0.1 M KOH. The carrier concentrations can be calculated by the slope derived from the Mott−Schottky plot.

$$\text{Slope} = \frac{2}{\varepsilon\varepsilon_0A^2e_0N_D} \quad (7)$$

where ε is the dielectric constant, ε_0 represents the vacuum permittivity, e_0 is the electronic charge, and A is the BET surface area of the COFs.

The turnover frequency (TOF) was calculated using the following equation

$$\text{TOF} = \frac{J \times A}{4 \times F \times N} \quad (8)$$

where j (A/cm^2) is the current density at a given overpotential, A is the geometric surface area of the ring electrode area, F is the Faraday constant, and n (mol) is the molar amount of Sulfur (S) (present in COFs) loaded on the GC electrode, which was calculated based on elemental analysis. All the S atoms were assumed to be active for 2e^- ORR and that is why the TOF value represents the lower limit values.

Crystal Structure Modeling. Structural modeling of 3D@BT_TPA-COF and 2D@BT_TPA-COF was built using the Materials Studio program (version 2017) employing the Visualizer module. Various nets are referenced from the RCSR database (Reticular Chemistry Structure Resource, http://www.rcsr.net). Unit cell dimensions were set to the theoretical parameters. The lattice model was geometrically optimized by using a force-field-based method (Forcite). Pawley refinement was done using the Reflex tool, a software package for crystal determination from experimental XRD patterns. Optimization of the lattice parameters was carried out iteratively until the convergent R_{wp} value and the overlay of the observed with refined profiles showed well-fitting considering asymmetric corrections, broadening parameters from crystallite size and lattice strain.

Based on the geometry of the building units and connection pattern, 3D@BT_TPA-COF, all the reasonable topologies (RCSR database) were built (*pts*, *ptt*, *pth*, *pti*, *pds*, *fgl* etc.). The lattice models (e.g., cell parameters, atomic positions, and total energies) were then fully optimized by using the Forcite method. Each structure was subjected to Pawley refinement by experimental PXRD.

Computational Electrochemistry. In this work, the density functional theory was performed with the DMol3 package to examine the active sites and ORR performance.[47] The Perdew, Burke, and Ernzerhof (PBE) functional with generalized gradient approximation (GGA) method was used

https://doi.org/10.1021/acsomega.5c00568
ACS Omega 2025, 10, 18829−18839

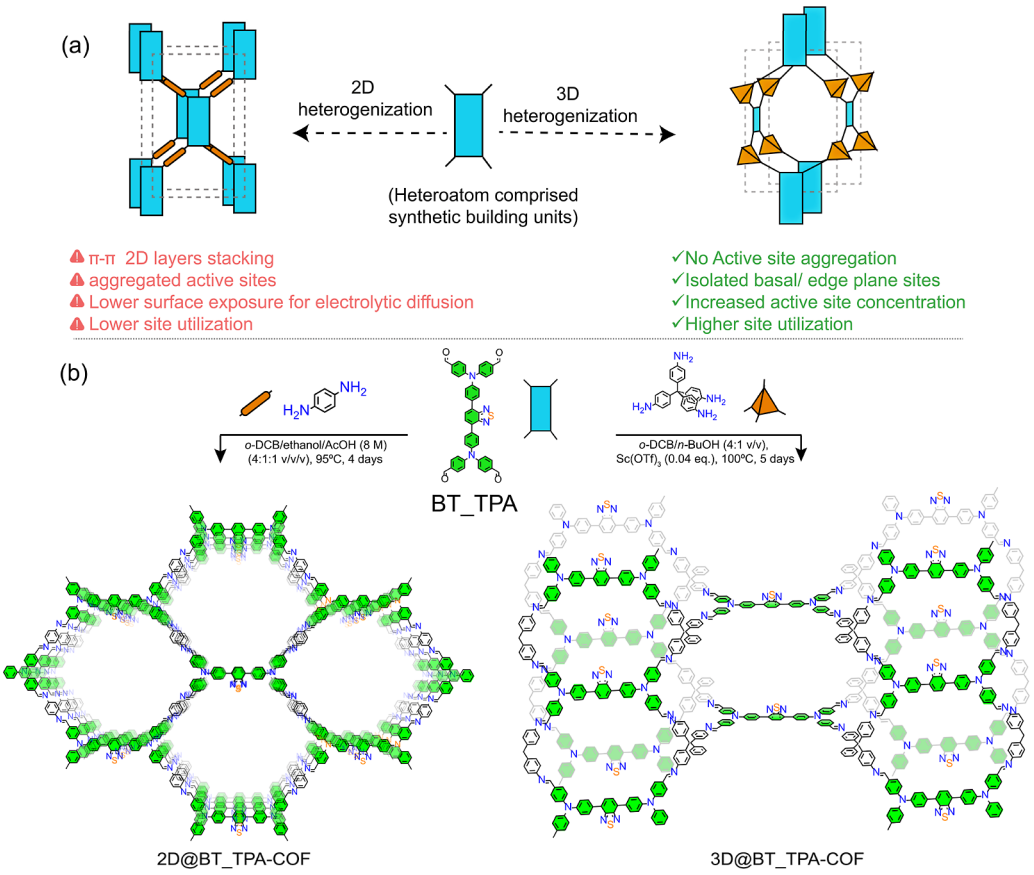

Figure 1. (a) Illustration of dimensional tunning and principle for designing 3D COF-based electrocatalyst system; (b) synthetic scheme for 2D@BT_TPA-COF and 3D@BT_TPA-COF sharing a common redox active building unit, BT_TPA.

to describe exchange−correlation interactions between electrons.[48] The dispersion interactions were treated by the Grimme scheme.[49] The double numerical plus polarization (DNP) basis sets were adopted with a global orbital cutoff of 4.5 Å. The energy and force convergences were set as 10×10^{-5} Ha and 0.002 Ha/Å, respectively. To simulate the solvent environment, the conductor-like screening model (COSMO) was done with a dielectric constant of 78.54.[50]

For the structural models, we initially optimized the periodic structure models, as depicted in experimental simulations (Figure S25). Due to the large cell parameters (2D: a = 29.57 Å, b = 44.8 Å, c = 9.55 Å; 3D: a = 17.93 Å, b = 18.04 Å, c = 55.11 Å), the Monkhorst−Pack method with a gamma point was used to sample reciprocal space.[51] Subsequently, we extracted the benzothiadiazole segment along with its surrounding environment using our computational molecular model. During this process, the outermost benzene rings and connected nitrogen atoms were fixed to maintain the structural integrity. To get the free energy diagram, the Gibbs free energy is calculated by

$$\Delta G = \Delta E + \Delta \mathrm{ZPE} - T\Delta S \quad (9)$$

where ΔE is the electronic energy difference between two catalytic intermediates. ΔZPE and ΔS are zero-point energy differences and entropy differences obtained from frequency calculations. The T presents a temperature set at 298.15 K (room temperature).

RESULTS AND DISCUSSION

3D@BT_TPA-COF was synthesized from solvothermal imine condensation between tetrakis(4-aminophenyl)methane (TAM) and BT_TPA in a stoichiometric ratio of 1:1 (Figure 1b). Higher crystallinity for the noninterpenetrated 3D@BT_TPA-COF structure was achieved in the *o*-DCB/*n*-butanol/$Sc(OTf)_3$ (4:1 and 0.04 equiv) mixture at 100 °C for 5 days (yield: ∼71%; Table S1, Figure S1). The 2D framework (2D@BT_TPA-COF) was synthesized from the condensation between *p*-phenylenediamine (PDA) and BT_TPA in a stoichiometric ratio of 2:1 in the *o*-DCB/ethanol/AcOH (8 M) AcOH (4:1:1) mixture at 95 °C for 4 days (yield: ∼75%; Table S3, Figure S4). The Fourier-transform infrared (FT-IR) spectroscopy and solid-state ^{13}C nuclear magnetic resonance (^{13}C CP/MAS NMR) spectroscopy were carried out to elucidate the functional information about the frameworks. FT-IR spectra of 3D@BT_TPA-COF and 2D@BT_TPA-COF showed the characteristic C═N stretching vibration at 1618 cm^{-1} and 1627 cm^{-1} respectively (Figure S6). The C═O stretching (1691 cm^{-1}) in the aldehyde monomer (BT_TPA) and −NH stretching in the amine monomers were significantly decreased in the resulting COFs. ^{13}C CP/MAS NMR spectra of 3D@BT-TPA-COF and 2D@BT-TPA-COF showed a peak around ∼152.2 and 152.9 ppm, respectively, which can be assigned for C═N functional groups (Figure 2a,b). X-ray photoelectron spectroscopy (XPS) was carried out to obtain more energetic information (different types of carbon, nitrogen, and sulfur) on 3D@BT_TPA-COF and 2D@BT_TPA-COF. N 1s XPS from each COF showed

https://doi.org/10.1021/acsomega.5c00568
ACS Omega 2025, 10, 18829−18839

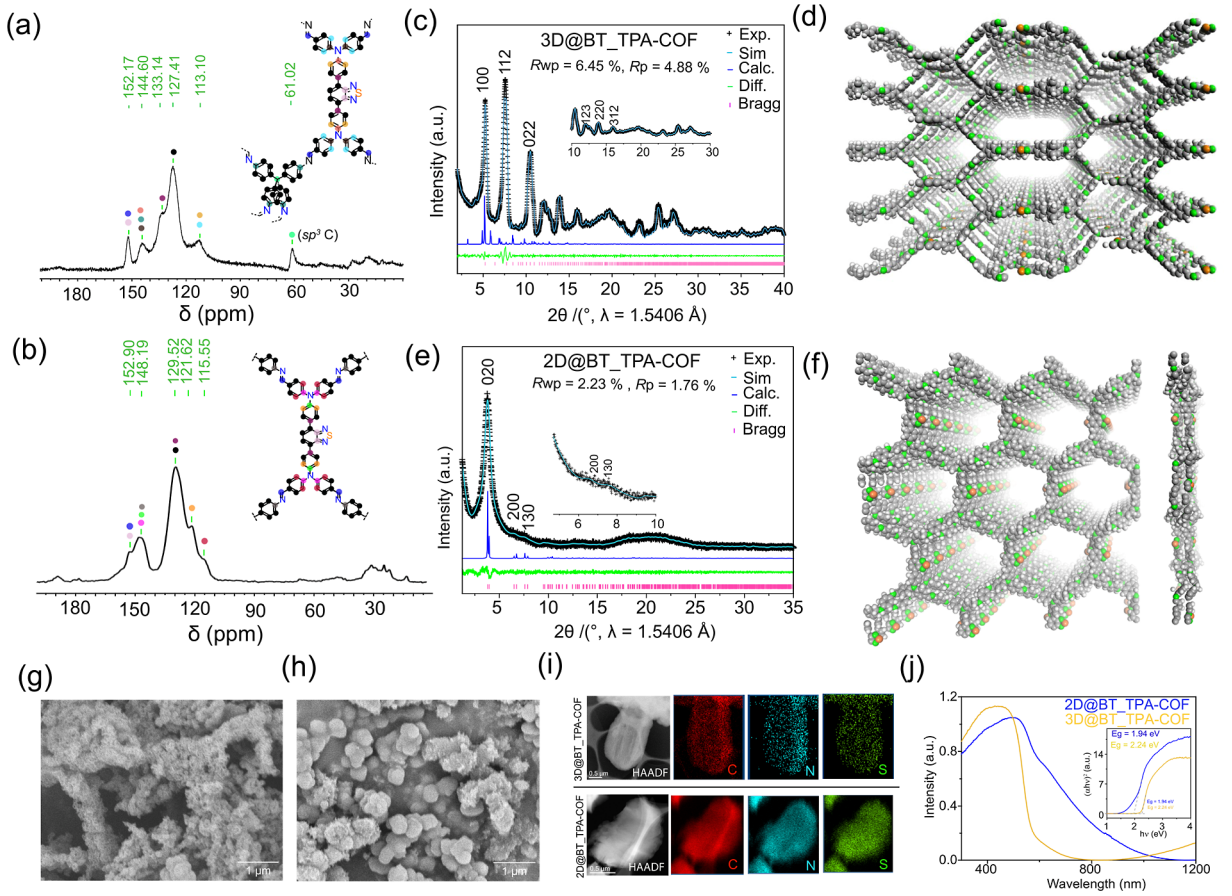

Figure 2. Characterizations of 3D@BT_TPA-COF and 2D@BT_TPA-COF. (a) Solid-state ^{13}C CP/MAS NMR of 3D@BT_TPA-COF and (b) of 2D@BT_TPA-COF; (c) PXRD simulation profile for 3D@BT_TPA-COF (Exp.: Experimental; Sim.: Simulated; Calc.: Calculated; Diff.: Difference; Bragg.: Bragg reflection); (d) simulated optimized model for 3D@BT_TPA-COF; (e) PXRD simulation profile for 2D@BT_TPA-COF and (f) top view and side view of simulated AA stacking of 2D@BT_TPA-COF where carbon has depicted as gray; nitrogen is green and sulfur is orange. Scanning electron microscopy images for 2D@BT_TPA-COF (g) and 3D@BT_TPA-COF (h); (i) HAADF image and elemental mapping of 3D@BT_TPA-COF and 2D@BT_TPA-COF; (j) UV/vis DRS spectra of 3D@BT_TPA-COF (yellow plot) and 2D@BT_TPA-COF (blue plot) (inset represents the optical band gap of both COFs from the Tauc plot).

three kinds of nitrogen from the triphenylamine, 2,1,3-benzothiadiazole (BTD) cores, and the imine functional regions (Figures S7, S8). Powder X-ray diffraction (PXRD) patterns of 3D@BT_TPA-COF and 2D@BT_TPA-COF exhibited amounts of diffraction peaks between 2F0E8 = 2 − 40F0B0 which indicates their crystalline nature. 3D@BT_TPA-COF showed the first reflection peak at 2θ = 5.3F0B0 and 2D@BT_TPA-COF showed at 2θ = 3.8F0B0. The lattice structures of both COFs were determined by comparing the experimental PXRD with the theoretical structure of other possible topologies (Figures S2, S3, and S5). The atomistic models of COFs were built and optimized using Accelrys Materials Studio 7.0 according to previous literature and the reticular chemistry structure resource (RCSR). Subsequently, the calculated PXRD was refined (Pawley) based on the constructed unit cell to get the simulated PXRD plot with a good agreement factor (*Rp*, *Rwp*) for both COFs. Several possible lattices (e.g., *pts, ptt, fgl, pds,* etc. with considering catenations) were built and optimized for 3D@BT_TPA-COF. Specifically, by considering the geometry of the building units and the packing orientations, the experimental PXRD for 3D@BT_TPA-COF was found to have an excellent match (*Rwp* = 6.45%, *Rp* = 4.88%) with the simulated pattern (cyan solid plot, Figure 2c,d) of 3D noninterpenetrated *pts* topology, in the space group, *PM* (*a* = 17.92 Å *b* = 18.04 Å, *c* = 55.10 Å; F0E1 = F0E3 = 90F0B0, F0E2 = 89.20F0B0). PXRD for 2D@BT_TPA-COF was found to have an excellent match (*Rwp* = 2.23%, *Rp* = 1.76%) with the simulated pattern of the 2D rhombus structure with eclipse (AA) stacking (cyan solid plot, Figure 2e,f), in the space group, *C*2 (*a* = 29.57 Å, *b* = 44.8 Å, *c* = 9.55 Å; F0E1 = F0E3 = 90F0B0, F0E2 = 112.89F0B0). In addition, the Brunauer−Emmett−Teller (BET) surface area of 2D@BT_TPA-COF and 3D@BT_TPA-COF was found to be 501 and 716 m^2/g with the pore size distribution centered at 2.6 and 1.3 Å, respectively (Figures S9 and S10). Scanning electron microscopy (SEM) was used to visualize the particle morphology of both COFs. 3D@BT_TPA-COF exhibits a disk shape morphology with a diameter between 400 and 600 nm, and 2D@BT_TPA-COF exhibits an aggregated loose block morphology.[52] Scanning electron microscopy images and EDS mapping demonstrate that the carbon, nitrogen, and sulfur atoms are homogeneously distributed in both COFs (Figure 2i). The optical band gap for 3D@BT_TPA-COF and 2D@BT_TPA-COF was estimated from the Ultraviolet/visible diffusion reflectance spectra (UV/vis DRS). The spectra for 2D@BT_TPA COF were red-shifted compared to those for 3D@BT_TPA-COF, indicating that the 2D framework

https://doi.org/10.1021/acsomega.5c00568
ACS Omega 2025, 10, 18829−18839

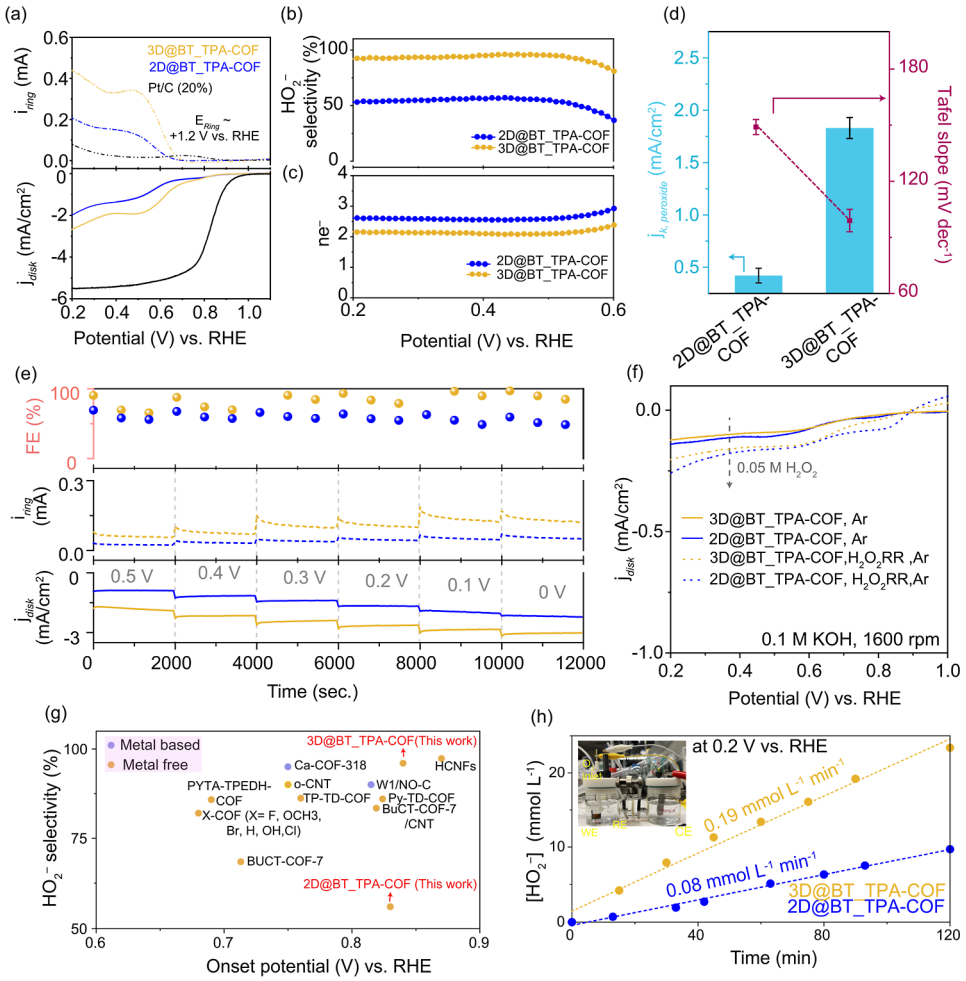

Figure 3. (a) Electrochemical oxygen reduction polarization curves (solid lines) at a rotation of 1600 rpm and simultaneous H_2O_2 detection currents on the ring electrode (dashed lines, current adjusted by collection efficiency) for 3D@BT_TPA-COF, 2D@BT_TPA-COF, and Pt/C (20%) in O_2-saturated 0.1 M KOH electrolyte; (b) H_2O_2 selectivity (%) and (c) calculated electron transfer number (n) of 3D@BT_TPA-COF and 2D@BT_TPA-COF based on the RRDE measurements; (d) kinetic current density (at 0.6 V vs RHE) and Tafel plots for 3D@BT_TPA-COF and 2D@BT_TPA-COF; (e) chronoamperometry (CA) profile for 3D@BT_TPA-COF (yellow solid line and dotted line denotes disk current and ring current, respectively) and 2D@BT_TPA-COF (blue solid line and dotted line denotes disk current and ring current respectively) at a potential range from 0.5 to 0 V in O_2 saturated 0.1 M KOH where yellow ball and blue ball shows the faradaic efficiency for 3D@BT_TPA-COF and 2D@BT_TPA-COF, respectively, across potential range; (f) polarization curves (1600 rpm) of H_2O_2RR recorded in Ar-saturated 0.1 M KOH electrolyte containing 0.05 M H_2O_2; (g) comparison of performance of peroxide production (0.1 M KOH) on 3D@BT_TPA-COF and 2D@BT_TPA-COF and other recently reported electrocatalysts based on RRDE performance map of onset potential and maximum peroxide selectivity; (h) bulk electrosynthesis of H_2O_2 at a cell output voltage of 0.1 V where the data points represent the measured H_2O_2 amount by colorimetric method at different time interval and dashed lines represents theoretical yields.

possesses a more extended π-conjugated system than that for the 3D framework (Figure 2j). Tauc plot analysis from the UV/vis spectra revealed the optical band gap for 2D@BT_TPA-COF (blue plot) and 3D@BT_TPA-COF (yellow plot) which was found to be 1.94 and 2.24 eV, respectively (inset of Figure 2j).

Before accessing the electrocatalytic activity of 2D@BT_TPA-COF and 3D@BT_TPA-COF, cyclic voltammetry (CV) of the molecular analog (4,4′-(benzo[c][1,2,5]-thiadiazole-4,7-diyl)bis(*N*,*N*-diphenylaniline)) was taken in anhydrous dichloromethane (DCM, 0.1 M Tetrabutylammonium hexafluorophosphate) under Ar. The compound showed multiple quasireversible redox states. Notably, the redox peak at 0.45 V vs ferrocene/ferrocenium (Fc/Fc^+) can be attributed to the triphenylamine core, while two redox peaks at (−2.13 V) and (−1.9 V) were observed due to doubly reduced species of benzothiadiazole (Figure S12).[53] These findings suggest that the functional unit could serve as an excellent electrochemical $2e^-$ redox mediator. Then 3D@BT_TPA-COF and 2D@BT_TPA-COF were employed for the O_2 electroreduction reaction in 0.1 M KOH electrolyte using the three-electrode system. Linear sweep voltammetry (LSV) (a) and CV (Figure S13) were recorded in Argon (Ar) and O_2-presaturated 0.1 M KOH for both COFs at 1600 rpm (scan rate 10 mV/s). During LSV, the O_2 reduction currents were measured on the disk electrode (solid line, i_{disk}), and HO_2^- oxidation current was collected using the Platinum ring electrode (i_{ring}), held at a fixed potential of 1.2 V versus reversible hydrogen electrode (vs RHE). The limiting current densities (j_{lim}) for 2D@BT_TPA-COF and 3D@BT_TPA-COF were 1.97 and 2.63 mA cm^{-2}, respectively. A commercial 20% Pt/C (Fuel cell store, USA) catalyst was tested as a reference sample, which exhibited a limiting disk current density close to 5.5 mA cm^{-2} with negligible ring current. Enhanced $2e^-$ ORR kinetics for

https://doi.org/10.1021/acsomega.5c00568
ACS Omega 2025, 10, 18829−18839

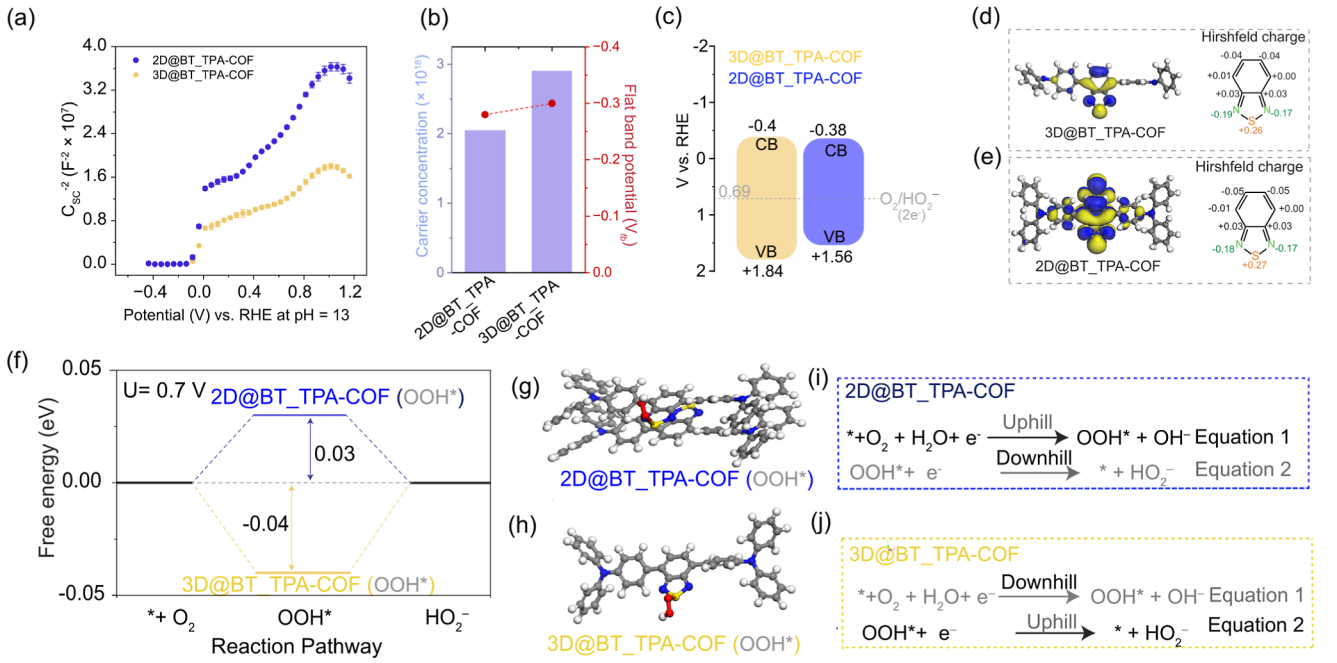

Figure 4. (a) Mott−Schottky plot of 3D@BT_TPA-COF (yellow plot) and 2D@BT_TPA-COF (blue plot) where the error bars represent the standard deviations of measurements taken three times for each COF; (b) N_D and V_{fb} of 2D@BT_TPA-COF and 3D@BT_TPA-COF; (c) valence band (VB) and conduction band (CB) for both COFs; (d) the LUMO of 3D@BT_TPA-COF (left side) with atomic Hirshfeld (right side) charge; (e) the LUMO of 2D@BT_TPA-COF (left side) with atomic Hirshfeld (right side) charge where the atoms are marked as white: hydrogen, gray: carbon, blue: nitrogen, and yellow: sulfur; (f) the free energy diagram of the 2e$^-$ ORR process. The yellow and blue lines correspond to the ORR process on 2D@BT_TPA-COF and 3D@BT_TPA-COF. Structure of OOH* intermediate for 2D@BT_TPA-COF and 3D@BT_TPA-COF where the atoms are marked as white: hydrogen, gray: carbon, blue: nitrogen, red: oxygen, and yellow: sulfur (g,h). Comparison of the two-step 2e$^-$ ORR pathway for both COFs (i,j).

3D@BT_TPA-COF compared to 2D@BT_TPA-COF can be understood from the disk current density (j_{disk}) that gives much higher currents and more positive onset potential (defined as the potential measured at a j_{disk} of −0.1 mA cm^{-2}). For the ring current, an onset potential of 0.68 V (defined as the potential measured at j_{ring} of 0.1 mA cm^{-2}) was observed for 3D@BT_TPA-COF close to the thermodynamic limit (0.70 V) whereas an onset potential of 0.63 V was observed for 2D@BT_TPA-COF. The i_{ring} from 3D@BT_TPA-COF was found to be almost 3 times higher than that of 2D@BT_TPA-COF at 0.5 V vs RHE. The double-layer capacitance (C_{dl}) for 3D@BT_TPA-COF was found to be 5.55 and 4.6 mF cm^{-2} for 2D@BT_TPA-COF (Figure S14). The water contact angle (CA) for 3D@BT_TPA-COF and 2D@BT_TPA-COF were found to be 109.3F0B0 and 127.6F0B0 (Figure S15), respectively, which implies that the 3D framework is more hydrophilic than 2D@BT_TPA-COF. The increased electrochemically active surface area (ECSA) and enhanced hydrophilicity of the 3D@BT_TPA-COF suggest that the 3D framework promotes more efficient electrolyte access to the active sites, significantly improving wettability. This, in turn, strengthens the electrode−electrolyte interface, facilitating better contact and potentially boosting electrochemical performance. In a wide potential range from 0.60 to 0.20 V, the HO_2^- selectivity of 2D@BT_TPA-COF catalyst was calculated (collection efficiency was calculated to be 21%, Figure S16) to be around 36−53% with n value 2.9−2.6 whereas 3D@BT_TPA-COF catalyst showed HO_2^- selectivity 91−96% with n value 2.0−2.1 (Figure 3b,c). The electron transfer number was further validated from the Koutecky−Levich (K−L) eq (Figure S17) by recording LSV at different rotation rates (400−2000 rpm). The kinetic current densities ($j_{k,peroxide}$) for 2D@BT_TPA-COF and 3D@BT_TPA-COF were calculated to be 0.42 and 1.83 mA cm^{-2}, respectively, at 0.6 V vs RHE. As shown in Figure 3d, the Tafel slope of 3D@BT_TPA-COF was found to be 99 mV dec^{-1}, lower than that for 2D@BT_TPA-COF (149 mV dec^{-1}, Figure S18). Mass activity vs ORR potential plot (Figure S19) demonstrates that 3D@BT_TPA-COF possesses a superior current-to-mass ratio than 2D@BT_TPA-COF. Faradaic efficiency for both COFs was systematically evaluated, at RRDE chronoamperometric (CA) conditions at different ORR potentials. As shown in Figure 3e, 3D@BT_TPA-COF shows an improved 2e$^-$ faradaic efficiency compared to that for 2D@BT_TPA-COF across the potential range from 0.5 to 0 V. It is worth mentioning that 3D@BT_TPA-COF follows a current efficient peroxide production over the broad potential range, indicating its potential for long-term robust electrolysis. Figure 3f compares voltammograms from the 3D@BT_TPA-COF and 2D@BT_TPA-COF catalysts in Ar-saturated 0.1 M KOH with externally added H_2O_2 (0.05 M). A small cathodic current was observed due to residual O_2 after Ar purging and the externally added H_2O_2 did not produce any significant H_2O_2RR current for 3D@BT_TPA-COF. It demonstrates that 3D@BT_TPA-COF is intrinsically inactive to further reduce H_2O_2. In comparison, 2D@BT_TPA-COF exhibited a slightly higher H_2O_2RR current than that for 3D structure which indicates the poor 2e$^-$ ORR. The onset potential and peroxide selectivity of both COFs were compared against previously reported outstanding catalysts (Figure 3g, Table S5). This comparison aims to illustrate the contrast between the 2D and 3D COFs, emphasizing how their dimensional variations influence their

https://doi.org/10.1021/acsomega.5c00568
ACS Omega 2025, 10, 18829−18839

2e$^-$ ORR selectivity. The stability of 3D@BT_TPA-COF and 2D@BT_TPA-COF was evaluated over five consecutive 1 h tests (~5 h total), showing negligible changes in activity and selectivity on both the ring and disc electrodes (Figure S20). During each cycle, the disc and ring electrodes were maintained at 0.5 V vs RHE and 1.3 V vs RHE, respectively. After each cycle, the ring electrode was cleaned, and a fresh electrolyte was introduced. To explore the possibility of practical implementation, both COFs were cast on carbon paper and installed in a two-compartment H-cell electrolyzer (separated by an anion exchange membrane) containing O_2-saturated 0.1 M KOH containing O_2 for the bulk electrolysis. To determine the faradaic efficiency (FE), the COF cast electrode was polarized at a constant potential of 0.1 V vs RHE for 120 min to accumulate a substantial amount of peroxide in the cathode compartment (Figures S21 and S22). The peroxide concentration was measured by a colorimetric cerium sulfate ($Ce(SO_4)_2$) titration method (Figure S23) based on the mechanism that H_2O_2 would reduce a yellow solution of Ce^{4+} to colorless Ce^{3+} ($2Ce^{4+} + H_2O_2 \rightarrow 2Ce^{3+} + 2H^+ + O_2$). The H_2O_2 production rate of 3D@BT_TPA-COF was calculated to be 0.8 mol g^{-1} h^{-1} with FE of 88%, and the value for 2D@BT_TPA-COF was found to be 0.1 mol g^{-1} h^{-1} with a FE of 41%.

Based on the experimental findings, we propose that reticular extension from 2D to noninterpenetrated 3D framework achieves enhanced peroxide selectivity in alkaline conditions. Electrochemical impedance spectroscopy (EIS) was done to understand the ion electrolyte diffusion in both COFs using the correlation diagram between Z′ and $\omega^{-1/2}$ at the open-circuit potential. The diffusion coefficients of hydroxyl ions (D_{OH^-}) for 3D@BT_TPA-COF were found to be 1.07×10^{-18} cm^2 s^{-1}, which is greater than that for 2D@BT_TPA-COF (7.72×10^{-19} cm^2 s^{-1}) (Figure S24). This demonstrates the increased electrolytic diffusion within the nanocavity of the 3D COF. This, in turn, facilitates effective interaction among the catalyst's pore walls, electrolyte, and gaseous O_2 molecules, resulting in the creation of an abundant three-phase interface.[54] Such conditions are favorable for the facile electroconversion of O_2. On the contrary, 2D COFs possess stacked layers that limit the exposure of ORR sites. The low free space volume leads to shorter residence time for O_2 molecules resulting in shorter diffusion pathways and consequently reducing the 2e$^-$ ORR activity. Motty−Schottky (M−S) analysis was carried out for 3D@BT_TPA-COF and 2D@BT_TPA-COF which indicates that they are n-type semiconductors with a positive slope (Figure 4a). The carrier concentration (N_D) and the flat band potential (V_{fb}) for both COFs were estimated from the slope of M−S plots (Figure S25) and the accompanying straight-line intercept with the x-axis. The V_{fb} for 3D@BT_TPA-COF and 2D@BT_TPA-COF was found to be −0.3 and −0.28 V vs RHE. The N_D for 3D@BT_TPA-COF (2.9×10^{18}) was found to be higher than 2D@BT_TPA-COF (2.05×10^{18}) which indicates the higher electron donor density of 3D@BT_TPA-COF compared to 2D@BT_TPA-COF (Figure 4b). The valence band (VB) and conduction band (CB) were estimated (Figure 4c) for both COFs based on UV/vis DRS and M-S plots. The CB position of 3D@BT_TPA-COF and 2D@BT_TPA-COF was estimated to be −0.4 and −0.38 V, respectively, considering the CB lies 0.1 V more negative than the V_{fb} position for n-type semiconductors. The V_{fb} and N_D values from the M-S plot imply that 3D@BT_TPA-COF have more upward band bending in the electrode/electrolyte interface and possess higher nucleophilic strength.[55,56] All of these observations demonstrate the importance of the topology and dimensionality in the strategic design of COFs to tune their electrochemical activity and selectivity. DFT calculations were employed to investigate the 2e$^-$ ORR activity of two COFs. A redox-active fragment based on benzothiadiazole/triphenylamine (Figure 4d,e, left) was extracted from the periodic structure as the computational model (Figure S26). Hirshfeld charge analysis (Figure 4d,e, right) was conducted to identify the potential electrophilic sites for O_2 binding, which are typically more reactive when they possess larger LUMO coefficients and have a significantly positive charge or spin density. Notably, the sulfur (S) atom in the benzothiadiazole unit located on pore walls could serve as a significant active site for oxygen binding. Based on the S atom, the turnover frequencies (TOFs) for 2D@BT_TPA-COF and 3D@BT_TPA-COF were calculated to be 0.042 s^{-1} and 0.061 s^{-1}, respectively, at 0.5 V (Figure S27). The 2e$^-$ ORR activity of the catalysts was assessed by calculating the free energy of the entire reaction involving two steps: $*+O_2 + e^- \rightarrow *OOH$ and $*OOH + e- \rightarrow *+HO_2^-$. Free energy change of the adsorption of OOH (ΔG^*_{OOH}) is a key descriptor for 2e$^-$ ORR. The asterisk (*) denotes active sites in the catalyst. The calculated ΔG^*_{OOH} values were approximately 4.18 and 4.24 eV for 3D@BT_TPA-COF and 2D@BT_TPA-COF (close to the ideal value of approximately 4.22 eV),[57] indicating that theoretically, both systems can provide a near-ideal environment for optimal OOH binding. Figure 4f illustrates that 2D@BT_TPA-COF possesses an uphill energy barrier (30 meV) to form the *OOH intermediate. In contrast, spontaneous formation of *OOH intermediate is possible on 3D@BT_TPA-COF at 0.7 V, followed by a small uphill (40 meV) step for the peroxide desorption from the catalyst surface, which demonstrates (Figure 4i,j) the improved activity of 3D@BT_TPA-COF over 2D@BT_TPA-COF for electrochemical peroxide production.

CONCLUSIONS

In summary, expanding the topology of a specific COF system from 2D to 3D enhances its electrocatalytic activity and selectivity for 2e$^-$ ORR. While 2D frameworks boast extensive π conjugation, the 3D counterpart offers superior access of the electrocatalytic site to the electrolyte, leading to an increased participation of active sites for electrocatalysis. This maximal exposure of active sites enhances mass transfer kinetics, improving overall activity and selectivity. This study provides novel insights into the electrocatalytic potential of higher-dimensional COFs.

ASSOCIATED CONTENT

Supporting Information

The Supporting Information is available free of charge at https://pubs.acs.org/doi/10.1021/acsomega.5c00568.

Detailed PXRD data with different reaction conditions; FTIR; BET plot; XPS plots; PXRD simulation information; and other electrochemical measurements (PDF)

https://doi.org/10.1021/acsomega.5c00568
ACS Omega 2025, 10, 18829−18839

AUTHOR INFORMATION

Corresponding Author

Carlos R. Cabrera − *Department of Chemistry and Biochemistry, University of Texas at El Paso, El Paso, Texas 79968, United States;* orcid.org/0000-0002-3342-8666; Email: crcabrerama@utep.edu

Authors

Subhajit Bhunia − *Department of Chemistry and Biochemistry, University of Texas at El Paso, El Paso, Texas 79968, United States; Department of Chemistry, University of Utah, Salt Lake City, Utah 84112, United States;* orcid.org/0000-0003-1135-4253

Linguo Lu − *Department of Chemistry, University of Puerto Rico, San Juan 00931, Puerto Rico;* orcid.org/0000-0002-0090-6764

Suzatra Chatterjee − *Department of Chemistry and Biochemistry, University of Texas at El Paso, El Paso, Texas 79968, United States*

Mounesha Garaga − *Department of Physics & Astronomy, Hunter College, City University of New York, New York, New York 10065, United States*

Alvaro Mayoral − *Instituto de Nanociencia y Materiales de Aragón (INMA), CSIC-Universidad de Zaragoza, Zaragoza 50009, Spain*

Ashley R. Head − *Center for Functional Nanomaterials, Brookhaven National Laboratory, Upton, New York 11973, United States;* orcid.org/0000-0001-8733-0165

Steven G. Greenbaum − *Department of Physics & Astronomy, Hunter College, City University of New York, New York, New York 10065, United States;* orcid.org/0000-0001-5497-5274

Zhongfang Chen − *Department of Chemistry, University of Puerto Rico, San Juan 00931, Puerto Rico;* orcid.org/0000-0002-1445-9184

Xiaowei Wu − *Fujian Institute of Research on the Structure of Matter, Xiamen Institute of Rare Earth Materials, Chinese Academy of Sciences, Xiamen 361021, China;* orcid.org/0000-0003-2141-3448

Complete contact information is available at: https://pubs.acs.org/10.1021/acsomega.5c00568

Author Contributions

$^{\nabla}$L.L. and S.C. contributed equally.

Notes

The authors declare no competing financial interest.

ACKNOWLEDGMENTS

C.R.C. acknowledges the Center for Alkaline-based Energy Solutions (CABES), an Energy Frontier Research Center funded by the U.S. Department of Energy (DOE), Office of Science, Basic Energy Sciences (BES), under Award # DESC0019445. A.M. acknowledges the Spanish Ministry of science through the Ramon y Cajal program (RYC2018-024561-I) and to the Gobierno the Aragon (Nanomidas group, code E13_23R). A.M. also acknowledges the use of instrumentation as well as the technical advice provided by the National Facility ELECMI ICTS node "Laboratorio de Microscopías Avanzadas" at the University of Zaragoza. Z.C. acknowledges the Department of Energy, Office of Basic Energy Sciences, USA, under Award Number DE-SC0023418. Z.C. also thanks the computational support from the Center for Nanophase Materials Sciences (CNMS), a US Department of Energy Office of Science User Facility operated at Oak Ridge National Laboratory, and resources of the National Energy Research Scientific Computing Center (NERSC), a US Department of Energy Office of Science User Facility located at Lawrence Berkeley National Laboratory, operated under Contract no. DE-AC02-05CH11231 using NERSC award BES-ERCAP0027465. This research used the Proximal Probes Facility of the Center for Functional Nanomaterials (CFN), which is a U.S. Department of Energy Office of Science User Facility, at Brookhaven National Laboratory under Contract no. DE-SC0012704

ABBREVIATION

meV, millielectronvolt

REFERENCES

(1) Diercks, C. S.; Yaghi, O. M. The Atom, the Molecule, and the Covalent Organic Framework. *Science* **2017**, *355*, No. eaal1585.

(2) Yaghi, O. M. Reticular Chemistry in All Dimensions. *ACS Cent. Sci.* **2019**, *5*, 1295−1300.

(3) Jiang, D. Covalent Organic Frameworks: An Amazing Chemistry Platform for Designing Polymers. *Chem.* **2020**, *6*, 2461−2483.

(4) Kandambeth, S.; Dey, K.; Banerjee, R. Covalent Organic Frameworks: Chemistry Beyond the Structure. *J. Am. Chem. Soc.* **2019**, *141*, 1807−1822.

(5) Guo, J.; Jiang, D. Covalent Organic Frameworks for Heterogeneous Catalysis: Principle, Current Status, and Challenges. *ACS Cent. Sci.* **2020**, *6*, 869−879.

(6) Geng, K.; He, T.; Liu, R.; Dalapati, S.; Tan, K. T.; Li, Z.; Tao, S.; Gong, Y.; Jiang, Q.; Jiang, D. Covalent Organic Frameworks: Design, Synthesis, and Functions. *Chem. Rev.* **2020**, *120*, 8814−8933.

(7) Huang, N.; Wang, P.; Jiang, D. Covalent Organic Frameworks: A Materials Platform for Structural and Functional Designs. *Nat. Rev. Mater.* **2016**, *1*, 16068.

(8) Li, L.-H.; Feng, X.-L.; Cui, X.-H.; Ma, Y.-X.; Ding, S.-Y.; Wang, W. Salen-Based Covalent Organic Framework. *J. Am. Chem. Soc.* **2017**, *139*, 6042−6045.

(9) Gropp, C.; Ma, T.; Hanikel, N.; Yaghi, O. M. Design of Higher Valency in Covalent Organic Frameworks. *Science* **2020**, *370*, No. eabd6406.

(10) An, S.; Lu, C.; Xu, Q.; Lian, C.; Peng, C.; Hu, J.; Zhuang, X.; Liu, H. Constructing Catalytic Crown Ether-Based Covalent Organic Frameworks for Electroreduction of CO_2. *ACS Energy Lett.* **2021**, *6*, 3496−3502.

(11) Lyu, H.; Li, H.; Hanikel, N.; Wang, K.; Yaghi, O. M. Covalent Organic Frameworks for Carbon Dioxide Capture from Air. *J. Am. Chem. Soc.* **2022**, *144*, 12989−12995.

(12) Stegbauer, L.; Hahn, M. W.; Jentys, A.; Savasci, G.; Ochsenfeld, C.; Lercher, J. A.; Lotsch, B. V. Tunable Water and CO_2 Sorption Properties in Isostructural Azine-Based Covalent Organic Frameworks through Polarity Engineering. *Chem. Mater.* **2015**, *27*, 7874−7881.

(13) Doonan, C. J.; Tranchemontagne, D. J.; Glover, T. G.; Hunt, J. R.; Yaghi, O. M. Exceptional Ammonia Uptake by a Covalent Organic Framework. *Nat. Chem.* **2010**, *2*, 235−238.

(14) He, L.; Chen, L.; Dong, X.; Zhang, S.; Zhang, M.; Dai, X.; Liu, X.; Lin, P.; Li, K.; Chen, C.; Pan, T.; Ma, F.; Chen, J.; Yuan, M.; Zhang, Y.; Chen, L.; Zhou, R.; Han, Y.; Chai, Z.; Wang, S. A Nitrogen-Rich Covalent Organic Framework for Simultaneous Dynamic Capture of Iodine and Methyl Iodide. *Chem.* **2021**, *7*, 699−714.

(15) Qiu, W.; Cui, J.; Zhu, K.; Gao, M.; Zheng, X.; Liu, H.; Guo, Z.; Zhang, Z.; Zhao, Y. Microenvironment Effect Catalysis with Phosphoric Acid-Based Covalent Organic Frameworks. *ACS Catal.* **2024**, *14*, 14780−14786.

(16) López-Magano, A.; Ortín-Rubio, B.; Imaz, I.; Maspoch, D.; Alemán, J.; Mas-Ballesté, R. Photoredox Heterobimetallic Dual

Catalysis Using Engineered Covalent Organic Frameworks. *ACS Catal.* **2021**, *11*, 12344−12354.
(17) Jati, A.; Dey, K.; Nurhuda, M.; Addicoat, M. A.; Banerjee, R.; Maji, B. Dual Metalation in a Two-Dimensional Covalent Organic Framework for Photocatalytic C−N Cross-Coupling Reactions. *J. Am. Chem. Soc.* **2022**, *144*, 7822−7833.
(18) Gutiérrez, L.; Martin-Diaconescu, V.; Casadevall, C.; Oropeza, F.; de la Peña O'Shea, V. A.; Meng, J.; Ortuño, M. A.; Lloret-Fillol, J. Low Oxidation State Cobalt Center Stabilized by a Covalent Organic Framework to Promote Hydroboration of Olefins. *ACS Catal.* **2023**, *13*, 3044−3054.
(19) Sun, M.-Y.; Cheung, S. C.; Wang, X.-Z.; Jin, J.-K.; Guo, J.; Li, D.; He, J. Structural Reassignment of Covalent Organic Framework-Supported Palladium Species: Heterogenized Palladacycles as Efficient Catalysts for Sustainable C−H Activation. *ACS Cent. Sci.* **2024**, *10*, 1848−1860.
(20) Lu, M.; Zhang, S.-B.; Li, R.-H.; Dong, L.-Z.; Yang, M.-Y.; Huang, P.; Liu, Y.-F.; Li, Z.-H.; Zhang, H.; Zhang, M.; Li, S.-L.; Lan, Y.-Q. 3D Covalent Organic Frameworks with 16-Connectivity for Photocatalytic $C(sp^3)-C(sp^2)$ Cross-Coupling. *J. Am. Chem. Soc.* **2024**, *146*, 25832−25840.
(21) Zhao, Y.; Xu, X.; Zhang, K.; Li, Z.; Wang, H.; Zhao, Y.; Qiu, J.; Wang, J. Designing Local Electron Delocalization in 2D Covalent Organic Frameworks for Enhanced Sunlight-Driven Photocatalytic Activity. *ACS Catal.* **2024**, *14*, 3556−3564.
(22) Wang, Z.; Wang, C.; Chen, Y.; Wei, L. Covalent Organic Frameworks for Capacitive Energy Storage: Recent Progress and Technological Challenges. *Adv. Mater. Technol.* **2023**, *8*, 2201828.
(23) Alahakoon, S. B.; Thompson, C. M.; Occhialini, G.; Smaldone, R. A. Design Principles for Covalent Organic Frameworks in Energy Storage Applications. *ChemSusChem* **2017**, *10*, 2116−2129.
(24) Wu, Y.; Yan, D.; Zhang, Z.; Matsushita, M. M.; Awaga, K. Electron Highways into Nanochannels of Covalent Organic Frameworks for High Electrical Conductivity and Energy Storage. *ACS Appl. Mater. Interfaces* **2019**, *11*, 7661−7665.
(25) Lin, C. Y.; Zhang, D.; Zhao, Z.; Xia, Z. Covalent Organic Framework Electrocatalysts for Clean Energy Conversion. *Adv. Mater.* **2018**, *30*, 1703646.
(26) Hou, S.; Ji, W.; Chen, J.; Teng, Y.; Wen, L.; Jiang, L. Free-Standing Covalent Organic Framework Membrane for High-Efficiency Salinity Gradient Energy Conversion. *Angew. Chem.* **2021**, *133*, 10013−10018.
(27) Liu, X.; Huang, D.; Lai, C.; Zeng, G.; Qin, L.; Wang, H.; Yi, H.; Li, B.; Liu, S.; Zhang, M.; Deng, R.; Fu, Y.; Li, L.; Xue, W.; Chen, S. Recent Advances in Covalent Organic Frameworks (COFs) as a Smart Sensing Material. *Chem. Soc. Rev.* **2019**, *48*, 5266−5302.
(28) Liu, M.; Fu, Y.; Bi, S.; Yang, S.; Yang, X.; Li, X.; Chen, G. Z.; He, J.; Xu, Q.; Zeng, G. Dimensionally-Controlled Interlayer Spaces of Covalent Organic Frameworks for the Oxygen Evolution Reaction. *Chem. Eng. J.* **2024**, *479*, 147682.
(29) Gong, C.; Yang, X.; Wei, X.; Dai, F.; Zhang, T.; Wang, D.; Li, M.; Jia, J.; She, Y.; Xu, G.; Peng, Y. Three-Dimensional Porphyrin-Based Covalent Organic Frameworks with stp Topology for an Efficient Electrocatalytic Oxygen Evolution Reaction. *Mater. Chem. Front.* **2023**, *7*, 230−237.
(30) Guo, Z.; Yang, S.; Liu, M.; Xu, Q.; Zeng, G. Construction of Core-Shelled Covalent/Metal−Organic Frameworks for Oxygen Evolution Reaction. *Small* **2024**, *20*, 2308598.
(31) Yang, X.; Li, X.; Liu, M.; Yang, S.; Xu, Q.; Zeng, G. Confined Synthesis of Dual-Atoms within Pores of Covalent Organic Frameworks for Oxygen Reduction Reaction. *Small* **2024**, *20*, 2306295.
(32) Martínez-Fernández, M.; Martínez-Periñán, E.; Royuela, S.; Martínez, J. I.; Zamora, F.; Lorenzo, E.; Segura, J. L. Covalent Organic Frameworks Based on Electroactive Naphthalenediimide as Active Electrocatalysts toward Oxygen Reduction Reaction. *Appl. Mater. Today* **2022**, *26*, 101384.
(33) Yang, Z.; Gao, Y.; Zuo, L.; Long, C.; Yang, C.; Zhang, X. Tailoring Heteroatoms in Conjugated Microporous Polymers for Boosting Oxygen Electrochemical Reduction to Hydrogen Peroxide. *ACS Catal.* **2023**, *13*, 4790−4798.
(34) Wang, J.; Zhu, W.; Meng, F.; Bai, G.; Zhang, Q.; Lan, X. Integrating Dual-Metal Sites into Covalent Organic Frameworks for Enhanced Photocatalytic CO_2 Reduction. *ACS Catal.* **2023**, *13*, 4316−4329.
(35) Liu, H.; Chu, J.; Yin, Z.; Cai, X.; Zhuang, L.; Deng, H. Covalent Organic Frameworks Linked by Amine Bonding for Concerted Electrochemical Reduction of CO_2. *Chem.* **2018**, *4*, 1696−1709.
(36) Liu, S.; Qian, T.; Wang, M.; Ji, H.; Shen, X.; Wang, C.; Yan, C. Proton-Filtering Covalent Organic Frameworks with Superior Nitrogen Penetration Flux Promote Ambient Ammonia Synthesis. *Nat. Catal.* **2021**, *4*, 322−331.
(37) Kim, J. H.; Kim, Y.-T.; Joo, S. H. Electrocatalyst Design for Promoting Two-Electron Oxygen Reduction Reaction: Isolation of Active Site Atoms. *Curr. Opin. Electrochem.* **2020**, *21*, 109−116.
(38) Siahrostami, S.; Verdaguer-Casadevall, A.; Karamad, M.; Deiana, D.; Malacrida, P.; Wickman, B.; Escudero-Escribano, M.; Paoli, E. A.; Frydendal, R.; Hansen, T. W.; Chorkendorff, I.; Stephens, I. E. L.; Rossmeisl, J. Enabling Direct H_2O_2 Production through Rational Electrocatalyst Design. *Nat. Mater.* **2013**, *12*, 1137−1143.
(39) Zhao, H.; Yuan, Z.-Y. Design Strategies of Non-Noble Metal-Based Electrocatalysts for Two-Electron Oxygen Reduction to Hydrogen Peroxide. *ChemSusChem* **2021**, *14*, 1616−1633.
(40) Perry, S. C.; Pangotra, D.; Vieira, L.; Csepei, L.-I.; Sieber, V.; Wang, L.; Ponce de León, C.; Walsh, F. C. Electrochemical Synthesis of Hydrogen Peroxide from Water and Oxygen. *Nat. Rev. Chem* **2019**, *3*, 442−458.
(41) Chang, Q.; Zhang, P.; Mostaghimi, A. H. B.; Zhao, X.; Denny, S. R.; Lee, J. H.; Gao, H.; Zhang, Y.; Xin, H. L.; Siahrostami, S.; Chen, J. G.; Chen, Z. Promoting H_2O_2 Production Via 2-Electron Oxygen Reduction by Coordinating Partially Oxidized Pd with Defect Carbon. *Nat. Commun.* **2020**, *11*, 2178.
(42) An, S.; Li, X.; Shang, S.; Xu, T.; Yang, S.; Cui, C. X.; Peng, C.; Liu, H.; Xu, Q.; Jiang, Z.; Hu, J. One-Dimensional Covalent Organic Frameworks for the $2e^-$ Oxygen Reduction Reaction. *Angew. Chem., Int. Ed.* **2023**, *62*, No. e202218742.
(43) Lin, G.; Ding, H.; Yuan, D.; Wang, B.; Wang, C. A Pyrene-Based, Fluorescent Three-Dimensional Covalent Organic Framework. *J. Am. Chem. Soc.* **2016**, *138*, 3302−3305.
(44) Han, B.; Jin, Y.; Chen, B.; Zhou, W.; Yu, B.; Wei, C.; Wang, H.; Wang, K.; Chen, Y.; Chen, B.; et al. Maximizing Electroactive Sites in a Three-Dimensional Covalent Organic Framework for Significantly Improved Carbon Dioxide Reduction Electrocatalysis. *Angew. Chem., Int. Ed.* **2022**, *61*, No. e202114244.
(45) Eads, C. N.; Zhong, J.-Q.; Kim, D.; Akter, N.; Chen, Z.; Norton, A. M.; Lee, V.; Kelber, J. A.; Tsapatsis, M.; Boscoboinik, J. A.; Sadowski, J. T.; Zahl, P.; Tong, X.; Stacchiola, D. J.; Head, A. R.; Tenney, S. A. Multi-Modal Surface Analysis of Porous Films under Operando Conditions. *AIP Adv.* **2020**, *10*, 085109.
(46) Zhao, Y.; Zhu, L.; Tang, J.; Fu, L.; Jiang, D.; Wei, X.; Nara, H.; Asahi, T.; Yamauchi, Y. Enhancing Electrocatalytic Performance Via Thickness-Tuned Hollow N-Doped Mesoporous Carbon with Embedded Co Nanoparticles for Oxygen Reduction Reaction. *ACS Nano* **2024**, *18*, 373−382.
(47) Delley, B. From Molecules to Solids with the $DMol^3$ Approach. *J. Chem. Phys.* **2000**, *113*, 7756−7764.
(48) Perdew, J. P.; Burke, K.; Ernzerhof, M. Generalized Gradient Approximation Made Simple. *Phys. Rev. Lett.* **1996**, *77*, 3865.
(49) Grimme, S. Semiempirical GGA-Type Density Functional Constructed with a Long-Range Dispersion Correction. *J. Comput. Chem.* **2006**, *27*, 1787−1799.
(50) Klamt, A.; Schüürmann, G. COSMO: A New Approach to Dielectric Screening in Solvents with Explicit Expressions for the Screening Energy and its Gradient. *J. Chem. Soc., Perkin Trans. 2* **1993**, 799−805.
(51) Monkhorst, H. J.; Pack, J. D. Special Points for Brillouin-Zone Integrations. *Phys. Rev. B* **1976**, *13*, 5188.

https://doi.org/10.1021/acsomega.5c00568
ACS Omega 2025, 10, 18829−18839

(52) Huo, J.; Luo, B.; Chen, Y. Crystalline Covalent Organic Frameworks from Triazine Nodes as Porous Adsorbents for Dye Pollutants. *ACS Omega* **2019**, *4*, 22504−22513.
(53) Axelsson, M.; Marchiori, C. F. N.; Huang, P.; Araujo, C. M.; Tian, H. Small Organic Molecule Based on Benzothiadiazole for Electrocatalytic Hydrogen Production. *J. Am. Chem. Soc.* **2021**, *143*, 21229−21233.
(54) Chen, Y.; Su, D.; Chen, Y.; Zhu, Z.; Li, W. Three-Phase Interface-Assisted Advanced Electrochemistry-Related Applications. *Cell Rep. Phys. Sci.* **2021**, *2*, 100602.
(55) Bott, A. W. Electrochemistry of Semiconductors. *Curr. Sep.* **1998**, *17*, 87−92.
(56) Yang, H. B.; Miao, J.; Hung, S.-F.; Chen, J.; Tao, H. B.; Wang, X.; Zhang, L.; Chen, R.; Gao, J.; Chen, H. M.; Dai, L.; Liu, B. Identification of Catalytic Sites for Oxygen Reduction and Oxygen Evolution in N-Doped Graphene Materials: Development of Highly Efficient Metal-Free Bifunctional Electrocatalyst. *Sci. Adv.* **2016**, *2*, No. e1501122.
(57) Liu, C.; Ding, R.; Yang, J.; Liu, S.; Chen, L.; Xu, Q.; Li, J.; Yin, X. Low-Voltage Hydrogen Peroxide Electrolyzer for Highly Efficient Power-to-Hydrogen Conversion. *ACS Sustain. Chem. Eng.* **2023**, *11*, 2599−2606.

https://doi.org/10.1021/acsomega.5c00568
ACS Omega 2025, 10, 18829−18839